Measurement of the $\bar{p}p \to \bar{\Lambda}\Lambda$ and $\bar{p}p \to \bar{\Sigma}^0\Lambda$ + c.c. reactions at 1.726 and 1.771 GeV/c

P. D. Barnes, G. Franklin, B. Quinn, R. A. Schumacher, and V. Zeps
Carnegie-Mellon University, Pittsburgh, Pennsylvania 15260

N. Hamann*
CERN, Geneva, Switzerland

W. Dutty, H. Fischer, J. Franz, E. Rössle, H. Schmitt, and R. Todenhagen
Universität Freiburg, Freiburg, Germany

R. v. Frankenberg, K. Kilian, W. Oelert, K. Röhrich, K. Sachs, T. Sefzick, and M. Ziolkowski
Institut für Kernphysik der KFA Jülich, Jülich, Germany

R. A. Eisenstein, P. G Harris, D. W. Hertzog, S. A. Hughes, P. E. Reimer, and R. L. Tayloe
University of Illinois, Urbana, Illinois 61801

W. Eyrich, R. Geyer, M. Kirsch, R. A. Kraft, and F. Stinzing
Universität Erlangen-Nürnberg, Nürnberg, Germany

T. Johansson and S. Ohlsson
Uppsala University, Uppsala, Sweden

(Received 24 June 1996)

Interest in the production of hyperon-antihyperon pairs following antiproton-proton annihilation stems largely from attempts to understand the nature of flavor production. To date the major focus of both the experimental and the theoretical effort has been on the $\bar{p}p \to \bar{\Lambda}\Lambda$ reaction. In this paper, we present data on the complementary channels $\bar{p}p \to \bar{\Sigma}^0\Lambda$ and $\bar{p}p \to \bar{\Lambda}\Sigma^0$. Events from the kinematically similar $\bar{p}p \to \bar{\Lambda}\Lambda$ reaction were obtained in parallel. The procedure to distinguish these three separate reactions is described and results for all channels are presented. These include the total and differential cross sections, hyperon polarizations, and spin correlation coefficients. Data were obtained at incident antiproton lab momenta of 1.726 and 1.771 GeV/c which correspond to excess kinetic energies in the $\bar{p}p \to \bar{\Lambda}\Sigma^0$ + c.c. reaction of 26 and 40 MeV, respectively, above threshold. Comparisons are made to earlier work at similar excess energies in the $\bar{p}p \to \bar{\Lambda}\Lambda$ channel. The low-energy regime has been highlighted in this experiment to reduce the complexity in the theoretical analysis. [S0556-2813(96)01612-3]

PACS number(s): 25.43.+t, 13.75.Cs, 14.20.Jn

I. INTRODUCTION

The experiment PS185 studies strangeness production in $\bar{p}p$ collisions using the Low Energy Antiproton Ring (LEAR) facility at CERN. With a maximum available beam momentum of 2.0 GeV/c and hyperon-antihyperon ($\bar{Y}Y$) thresholds of 1.435, 1.653, and 1.853 GeV/c for $\bar{\Lambda}\Lambda$, $\bar{\Lambda}\Sigma$, and $\bar{\Sigma}\Sigma$, respectively, many of the experiments have been conducted in the low-energy regime. Using an energy scale defined by the excess energy ϵ above reaction threshold ($\epsilon = \sqrt{s} - m_Y - m_{\bar{Y}}$), studies are considered to be in the near-threshold regime if ϵ is in the order of a few MeV. Here, the cross section [1,2] (and the accumulated number of events) are low.

The $\bar{\Lambda}\Lambda$ cross section rises rapidly from threshold and peaks at about 80 μb and then begins to fall gently with further increasing energy. Data sets with large numbers of events have been accumulated by our collaboration at excess energies in the range of approximately ϵ = 13 – 200 MeV [3–5]. These data reveal detailed insights into the partial-wave evolution of the channel, the polarization nature of the outgoing hyperons and the spin correlation coefficients. A low-energy subset of the data has been used to extract a high-precision value for the $\Lambda\bar{p}K$ coupling constant [6]. Additionally use of the complete $\Lambda\Lambda$ data set is found in tests of CP and CPT symmetries through the analysis of the Λ and $\bar{\Lambda}$ decays [5,7].

The data can be summarized using model-independent amplitude analyses [8–11] which highlight the general features of the reaction. Attempting to delve deeper into the physics of flavor production, both meson exchange (MEX) [12–21] and quark-gluon (QG) [22–34] models have been used and are capable of reproducing the essential features of the low-energy PS185 data. In these models, different strangeness exchange microscopic processes are implied. In the MEX picture K, K^*, and even K^{**} mesons have been used to calculate exchange forces in the t channel between

*Deceased.

 © 1996 The American Physical Society

initial-state nucleons. Interference effects arising from the multiple mechanisms considered are found to be important. In the QG approach, both the $^3S_1$ and $^3P_0$ models have been used alone and in combination. The former implies a vector-like interaction possibly indicative of a $\overline{uu}\rightarrow\overline{ss}$ one- or odd-numbered gluon exchange. The latter would imply zero- or even-numbered gluon exchange with vacuum quantum numbers. The final-state interaction (FSI) parameters play a vital role in enabling good fits to be obtained to the data for either class of models.

It cannot be argued that one type of model is correct and the other wrong. What one would like to know is whether one of the classes of models is better able to capture the essence of the dominant underlying physics in the momentum transfer ($\approx$600 MeV/c) and distance-scale ($\approx\frac{1}{3}$ fm) regime where the hyperon-antihyperon production process takes place.

Continued growth in the low-energy $\overline{\Lambda}\Lambda$ data set alone does not appear to be capable of penetrating the issue further. However insight may be gained in the comparison of additional final-state channels such as $\overline{\Lambda}\Sigma$ or $\overline{\Sigma}\Sigma$. Such studies are motivated in part by the recognition that in kaon exchange models, the expected strength of the coupling constants differs significantly for Λ and Σ hyperons. For example, in pure SU(3), the ratio of the coupling constants in the respective hyperon-nucleon-kaon vertices is $(f^2_{\Sigma NK}/f^2_{\Lambda NK})=1/27$. The comparison of these coupling constants is very sensitive to the $\alpha=F/(F+D)$ ratio, here taken from SU(6) symmetry to be 0.4. Using the value obtained from weak interactions of $\alpha=0.355$, one is led to a ratio of the squares of the coupling constants of approximately 1/11. In either case, the implication is that the heavier K^* meson (whose coupling is also suppressed, but less so) plays a more prominent role and therefore the reaction may proceed on a shorter distance scale. A second thrust is to include additional observables such as the spin transfer, D_{nn} [21,25]. Such measurements introduce considerable experimental challenge and constitute the bulk of the remaining work of the PS185 collaboration.

The first of our non-$\overline{\Lambda}\Lambda$ hyperon-antihyperon studies was reported for the $\overline{p}p\rightarrow\overline{\Lambda}\Sigma^0+$c.c. reactions at an excess energy of $\approx$15 MeV [35]. The event sample was limited; accordingly, the extracted spin observables were not statistically significant. However the data reveal strong forward peaking in the differential cross section as is characteristic of the $\overline{p}p\rightarrow\overline{\Lambda}\Lambda$ reaction. For $\overline{p}p\rightarrow\overline{\Lambda}\Sigma^0+$c.c., the differential cross section hints at a richer partial-wave structure as we expect since the reaction is not self-conjugate. In this paper, we present an enlarged event sample of the $\overline{p}p\rightarrow\overline{\Sigma}^0\Lambda+$c.c. reactions at the incident antiproton momenta of 1.726 and 1.771 GeV/c. This corresponds to excess energies of 26 and 40 MeV, respectively. The momentum choices were made to facilitate comparison with previously reported results [3,4] on the complementary $\overline{p}p\rightarrow\overline{\Lambda}\Lambda$ reaction at similar excess energies. This serves to reduce the effects of both phase space differences and, to some degree, final-state interactions. The work significantly extends our initial investigation [35] into these channels since here we have obtained the necessary number of events to extract the spin observables of the system. Of particular interest is the possibility to extract the ΣNK coupling constant. We report 122 additional low-energy data points for the $\overline{p}p\rightarrow\overline{\Lambda}\Sigma^0+$c.c. reactions. To be useful in the coupling constant analysis, the condition that scattering occur to mainly S, P, and D final states must be met [6].

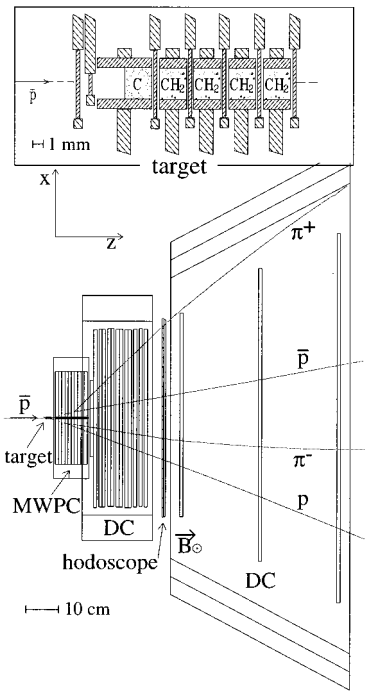

FIG. 1. The PS185 detector and target system.

We also report new and precise data on the $\overline{p}p\rightarrow\overline{\Lambda}\Lambda$ reaction obtained in parallel at the same incident momenta but corresponding to excess energies of $\approx$103 and 119 MeV.

II. EXPERIMENT

The PS185 apparatus is a nonmagnetic kinematic spectrometer situated on an extraction line of the LEAR facility at CERN. It is designed to measure reactions of the type $\overline{p}p\rightarrow\overline{\Lambda}\Lambda\rightarrow\overline{p}\pi^+p\pi^-$ by precise determination of the geometries of the two neutral decays (V^0 events) which are located downstream of the production point. With the substitution of a Σ^0 hyperon for the Λ in the above reaction (or the equivalent antiparticles), the same final charged-particle state is realized. The gamma from the prompt electromagnetic decay, $\Sigma^0\rightarrow\Lambda\gamma$ does not need to be measured in order to distinguish the channels as long as the precision on the charged-particle tracking is sufficient.

The essential features of the spectrometer include the triggering and tracking subsystems. These are shown in Fig. 1 and are described in more detail in Refs. [4,36]. The production of hyperon-antihyperon pairs occurs in a compact and segmented target which features five independent 2.5 mm diameter by 2.5 mm long cylindrical cells. Each cell is sandwiched between, and surrounded by, thin scintillators. A neutral target event is defined as one in which an antiproton enters a particular target cell and no charged particle exits. The signals from the scintillators are used in appropriate combinations to form the basis for this charged-particle veto and further for the determination of the event production

point. Of the five cells, four are made of CH_2 and one is pure carbon. The carbon cell is used to obtain a sample of data which reflects the kinematics and rate of those background events which naturally occur in the carbon component of the main CH_2 cells.

Upstream of the targets, four planes of silicon microstrip detectors are used to establish the direction of the incoming antiproton. The magnitude of the antiproton momentum is given by LEAR. The spread in incoming momenta is less than 0.2 MeV/c. The central value of the actual momenta at each target cell is computed from the extracted momentum less the losses through the upstream detectors and target cells.

The produced Λ and $\overline{\Lambda}$ decay downstream of the target system in a decay volume sufficient in size to contain the vertices and to permit adequate tracking of the emitted charged particles. The decay proton and antiproton are kinematically constrained to pass through a multielement scintillator hodoscope which is located at the end of the decay volume. The signal from this hodoscope, in coincidence with a neutral target event, forms the final experimental trigger selecting the events for which the raw data are recorded on magnetic tape. The decay volume is instrumented with two tracking detector subsystems. A set of 10 multiwire proportional chambers with alternating planes measuring the $u-v$ coordinates of passing charged particles is followed by a set of 13 drift chamber planes which establish the $x-y$ coordinates. Here, positive z is in the nominal beam direction, y is vertical and x is horizontal. The u and v coordinates are rotated at 45° with respect to x and y.

A final set of three drift chamber planes is housed in a $0.09T$ solenoid whose field is aligned parallel to the y direction. The size and location of the magnet is such that all decay baryons and many of the decay pions will pass through its volume. The trajectories of the tracks through the magnet are curved with a radius dependent on the magnitude of the horizontal component of the particle momentum and on its charge. The sign of the track curvature is used in the baryon number identification scheme. Since more than one particle must pass through the magnet, built in redundancy exists in the identification process.

III. DATA ANALYSIS

A. Event selection

The $\overline{p}p \to \overline{\Lambda}\Lambda$, $\overline{p}p \to \overline{\Sigma}^0\Lambda$, and $\overline{p}p \to \overline{\Lambda}\Sigma^0$ events of interest were selected from the raw data sample by applying cuts that selected for the appropriate and characteristic production and decay topologies. All selected events featured the two delayed decays, $\Lambda \to p\pi^-$ and $\overline{\Lambda} \to \overline{p}\pi^+$. The prompt decay $\Sigma^0 \to \Lambda\gamma$ implies that the $\overline{p}p \to \overline{\Sigma}^0\Lambda$+c.c. reactions form a subset of the final event sample and were automatically included in our event-selection procedure.

The following geometric and kinematic criteria were used for the first selection of candidate events. They were verified to be optimal by analyzing a subset of the data with only the kinematic fit analysis (described below) and checking the relevant distributions.

(1) The hit pattern of scintillators in the target array was consistent with the hypothesis that an antiproton entered the target and only neutral particles exited.

(2) The reconstructed tracks formed at least two V^0 patterns that passed the following tests.

(a) The V^0 was formed from two tracks that had a distance of closest approach within five times the error calculated for that quantity (5σ). This criteria was sufficiently wide to pass all true V^0's (with some large point scatters), yet cut spurious combinations.

(b) The vertex point was at least 1.0 cm downstream of the assigned production point of the hyperons. This was the minimum distance for which the individual reaction channels could be sufficiently separated.

(c) The vertex point was within a fiducial cone defined by the kinematics of $\overline{\Lambda}\Lambda$ or $\overline{\Sigma}^0\Lambda$+c.c. production. This cut eliminated nonphysical track combinations.

(d) The V^0 was coplanar with the production point to within 1.5 cm. These momentum cuts were appropriate to reject momentum-unbalanced V^0 pairs, yet pass combinations due to the events of interest (the momenta carried by the sigma-decay gamma is less than these cuts).

(3) The event contained at least one pair of V^0 patterns that, when combined, satisfied momentum conservation to within 0.15 GeV/c along the $\hat{x}$ and $\hat{y}$ axes and to within 0.35 GeV/c along $\hat{z}$. These momentum cuts were determined to be sufficient to reject momentum-unbalanced V^0 pairs.

Events that passed the V^0 constraints listed above were then subjected to a kinematic fit procedure which minimized a ''sum of squares,'' (X^2), subject to spatial, momentum, and energy constraints. For each event and for each candidate V^0 pair in the event, the procedure was performed for both the $\overline{p}p \to \overline{\Lambda}\Lambda$ and $\overline{p}p \to \overline{\Sigma}^0\Lambda$+c.c. reaction hypotheses. The $\overline{p}p \to \overline{\Sigma}^0\Lambda$+c.c. hypothesis was imposed twice for each V^0 pair; once with each of the two V^0's considered as that resulting from the Σ^0 decay Λ (the γ direction and energy was unmeasured in this procedure). The prefered reaction hypothesis and V^0 pair was chosen as that with the lowest resulting X^2 value. If this ''best-fit'' X^2 value was less than 18.5 for a $\overline{p}p \to \overline{\Lambda}\Lambda$ hypothesis or 15.1 for $\overline{p}p \to \overline{\Sigma}^0\Lambda$+c.c. (these values correspond to a χ^2 probability of 99% for the number of degrees of freedom in each fit), the event was retained and assigned to the appropriate reaction channel. The best-fit X^2 values for the two reaction channels are shown together with Monte Carlo data and the theoretical χ^2 functions in Fig. 2.

The two V^0's of the accepted event were then assigned a baryon number (i.e., to be a Λ or a $\overline{\Lambda}$) based on the information collected with the drift chamber situated in the magnetic solenoid. Tracks were recognized in this detector by collecting hits around the direction predicted by the results from the kinematic fit. For each track, a left- or right-bending assignment was made by picking the combination of hits near the track that best satisfied the hypothesized trajectory. With all particle tracks for which an assignment could be made, a sum of the track deflection distances was formed with an opposite weighting for V^0 baryon number assignment. If the absolute value of this sum was greater than 0.05 cm then the event was accepted and each V^0 was assigned a baryon number based on the sign of the sum.

After this analysis procedure, each event that passed all stages was assigned to be either a $\overline{p}p \to \overline{\Lambda}\Lambda$, $\overline{p}p \to \overline{\Sigma}^0\Lambda$, or

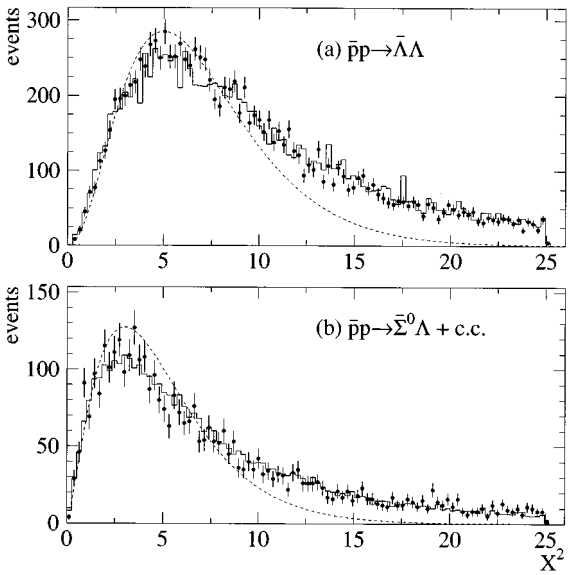

FIG. 2. The kinematic best-fit least-squares distributions for (a) $\overline{p}p \to \overline{\Lambda}\Lambda$, and (b) $\overline{p}p \to \overline{\Sigma}^0\Lambda$ + c.c. events for experimental (solid points) and Monte Carlo (solid line) data at 1.726 GeV/c. The Monte Carlo data have been normalized to have an equal number of events as the experimental data. The curves (dotted) are the expected χ^2 functions resulting from a fit with the correct number of degrees of freedom. They have been normalized to the bin with the maximum number of experimental events. The deviation of the theoretical χ^2 curves from the data and Monte Carlo distributions are due to the understood non-Gaussian response of the detector.

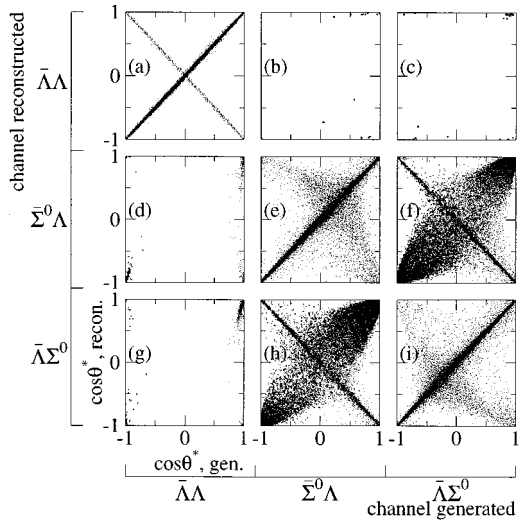

FIG. 3. A Monte Carlo study of the channel identification probability at 1.726 GeV/c. The three scatter plots of a given column represent generated events of a specific channel ($\Lambda\Lambda$, $\bar{\Sigma}^0\Lambda$, or $\Lambda\Sigma^0$), while those in a given row represent reconstructed events of a specific channel. Distributions (a), (e), and (i) contain events where the generated channel is the same as the reconstructed channel. All other distributions represent misidentified events. Each acceptably generated event may have at most one ''best'' solution.

$\overline{p}p \to \overline{\Lambda}\Sigma^0$ event and a unique c.m. production angle calculated. The reliability of these assignments is discussed below.

B. Acceptance calculation

The acceptance of the detector was calculated with a detailed simulation using the GEANT Monte Carlo package [37]. The complete geometry and the measured responses of each detector element were incorporated into the simulation. Approximately 800 000 events were generated for each reaction channel and momentum. Results from the Monte Carlo data were compared to those from the experimental data at all intermediate stages in the analysis (track-fitting, V^0 formation, etc.). As evidence for the quality of the simulation, the kinematic fit least-squares sum distributions for experimental and Monte Carlo data for the $\overline{p}p \to \overline{\Lambda}\Lambda$ and $\overline{p}p \to \overline{\Sigma}^0\Lambda$ + c.c. reaction channels are shown in Fig. 2 along with the theoretical χ^2 distributions. Deviations from the theoretical distributions are due to non-Gaussian responses inherent in the detector.

A nonnegligible fraction of events may be incorrectly assigned to a specific reaction channel and/or a c.m. scattering angle. This is due to the kinematic similarity of the $\overline{p}p \to \overline{\Lambda}\Lambda$, $\overline{p}p \to \overline{\Sigma}^0\Lambda$, and $\overline{p}p \to \overline{\Lambda}\Sigma^0$ reaction channels combined with the finite resolution of the apparatus and the possibility of misassignment of the baryon number.

The nature of cross-channel feedthrough was studied using the Monte Carlo data. The results are shown in the nine scatter plots in Fig. 3. Each plot displays the $\cos\theta^*$ of a *generated* channel versus the $\cos\theta^*$ of a *reconstructed* channel, where θ^* represents the c.m. angle of the antihyperon. The nine plots contain all of the possibilities for each of the three generated channels to be reconstructed as any of the three reconstructed channels. In this presentation, perfect channel assignment corresponds to entries in the plots along the diagonal [Figs. 3(a), 3(e), or 3(i)]. Within a correctly assigned plot, entries with the proper baryon number assignment fall along the line $\cos\theta^*_{\text{generated}} = \cos\theta^*_{\text{reconstructed}}$.

Entries in any of the other plots reflect incorrect channel assignment. Note that the incorrect assignment tends to populate particular angular regions within the plots. An acceptance matrix method [38] was developed to correct for this problem. From the Monte Carlo data, an initial acceptance matrix was formed that quantified the reaction channel and $\cos\theta^*$ misidentification. Then, using the *experimental distributions* (which are not flat) and an iterative inversion procedure [36,39], an acceptance function that properly disentangles the event misidentification was calculated for each reaction channel. The resulting acceptance, when averaged over $\cos\theta^*$, is 13% for $\overline{p}p \to \overline{\Lambda}\Lambda$ and 16% for $\overline{p}p \to \overline{\Sigma}^0\Lambda$ + c.c. at 1.726 GeV/c and falls slightly to 11% and 13%, respectively, at 1.771 GeV/c. This function could then be used to produce the corrected $\cos\theta^*$ event distributions.

As can be seen by the off-diagonal scatter plots in Fig. 3, imperfections in the channel identification procedure exist at a nonnegligible level. Misidentification of $\overline{\Lambda}\Lambda$ events as $\Lambda\Sigma^0$ or $\overline{\Sigma}^0\Lambda$ is a problem compounded further by the asymmetry of the misidentification of the events [compare Figs. 3(d) and 3(g)]. The forward $\overline{\Lambda}\Lambda$ events are more likely to be misidentified as $\overline{\Lambda}\Sigma^0$ events while the backward $\overline{\Lambda}\Lambda$ events flow dominantly to $\overline{\Sigma}^0\Lambda$. Since the $\overline{p}p \to \overline{\Lambda}\Lambda$ reaction is

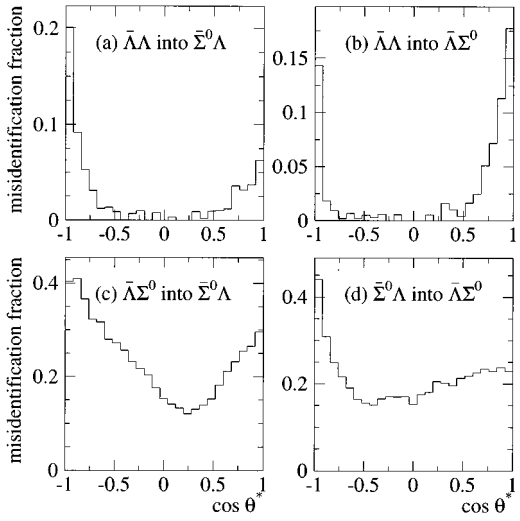

FIG. 4. Calculated fraction in each $\cos\theta^*$ bin of (a) $\overline{p}p \to \overline{\Sigma}^0\Lambda$ or (b) $\overline{p}p \to \overline{\Lambda}\Sigma^0$ events that are due to incorrectly identified $\overline{p}p \to \overline{\Lambda}\Lambda$ events. Calculated fraction of (c) $\overline{p}p \to \overline{\Sigma}^0\Lambda$, or (d) $\overline{p}p \to \overline{\Lambda}\Sigma^0$ that are due to incorrectly identified charge conjugate events. The study was performed at an incident antiproton momentum of 1.726 GeV/c.

forward peaked, a greater contamination exists in the $\overline{\Lambda}\Sigma^0$ channel compared to the $\overline{\Sigma}^0\Lambda$ channel. For true $\overline{p}p \to \overline{\Sigma}^0\Lambda$ or $\overline{p}p \to \overline{\Lambda}\Sigma^0$ events, misidentification can cause an event to be recorded as its charge-conjugate channel. Once again, the distribution of misidentified events is not uniform in $\cos\theta^*$. Projections of the misidentification fractions as calculated using the acceptance matrix method for the most affected channels are shown in Fig. 4. These plots show the calculated fraction of events assigned to a reaction channel at a given $\cos\theta^*$ that are from the incorrect channel.

To check the accuracy of the channel identification procedure and to estimate the systematic error, the differential cross section distributions for $\overline{p}p \to \overline{\Sigma}^0\Lambda$ and $\overline{p}p \to \overline{\Lambda}\Sigma^0$ were considered separately. Charge-conjugation invariance of the strong-interaction hyperon-production process implies that they must be equivalent. The fractional difference, δ, in the differential cross sections, defined as

$$\delta = \left(\frac{d\sigma}{d\Omega}(\overline{\Sigma}^0\Lambda) - \frac{d\sigma}{d\Omega}(\overline{\Lambda}\Sigma^0) \right) \Bigg/ \left(\frac{d\sigma}{d\Omega}(\overline{\Sigma}^0\Lambda) + \frac{d\sigma}{d\Omega}(\overline{\Lambda}\Sigma^0) \right),$$

is shown in Fig. 5 for both momenta. The indicated errors include statistical errors only. These distributions support the conclusion that the acceptance calculation is sound. It was estimated that the systematic error on the acceptance as a function of $\cos\theta^*$ was a constant 2% plus 5% times the event misidentification fraction. This yields a systematic error, averaged over $\cos\theta^*$ of 2.3% for $\overline{p}p \to \overline{\Lambda}\Lambda$ and 3.6% for the $\overline{p}p \to \overline{\Sigma}^0\Lambda$+c.c. channels. These errors were propagated through to subsequent results.

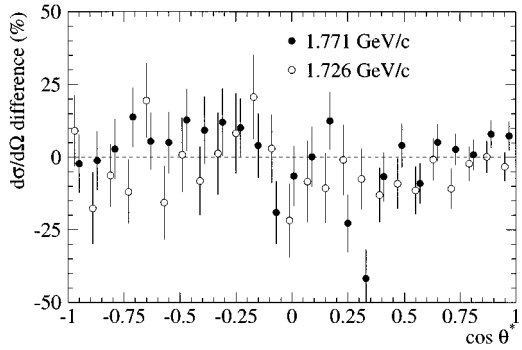

FIG. 5. Fractional difference in the measured differential cross sections defined as $\delta = [(d\sigma/d\Omega)(\overline{\Sigma}^0\Lambda) - (d\sigma/d\Omega)(\overline{\Lambda}\Sigma^0)]/[(d\sigma/d\Omega)(\overline{\Sigma}^0\Lambda) + (d\sigma/d\Omega)(\overline{\Lambda}\Sigma^0)]$ for the $\overline{p}p \to \overline{\Sigma}^0\Lambda$ and $\overline{p}p \to \overline{\Lambda}\Sigma^0$ reactions at 1.726 and 1.771 GeV/c. The points have been offset horizontally to avoid overlap. The errors are statistical only.

C. Calculation of the cross section

The final cross sections were obtained from the acceptance-corrected measured event distributions, the integrated luminosity, and the following correction factors.

(1) The double branching ratio factor for both Λ hyperons to decay into p, π is 0.4083 ± 0.0064 [40].

(2) The fraction of events rejected by the trigger due to the production of a δ-ray electron and subsequent veto in the target accounts for a 1% normalization correction.

(3) The fraction of events rejected by a veto from an additional beam antiproton in the trigger time window required a rate-dependent correction. This correction varied with each target cell, averaging 8.5% overall.

(4) The number of events accepted that were the result of production on a carbon nucleus in the CH_2 target cells could be estimated using the pure carbon cell. Assuming that the angular distributions of the carbon events are similar to those on free protons results in a correction of 2.5% for $\overline{p}p \to \overline{\Lambda}\Lambda$ events and 14.1% for $\overline{p}p \to \overline{\Sigma}^0\Lambda$+c.c. events.

(5) The average lifetime of the data acquisition system was 72.5%.

The integrated luminosity on the four CH_2 target cells was $4.54 \pm 0.09 \times 10^3$ μb^{-1} at 1.726 GeV/c and $6.44 \pm 0.13 \times 10^3$ μb^{-1} at 1.771 GeV/c. The quoted errors are dominated by the systematic error which includes the uncertainties on the above correction factors with the exception of the branching ratio.

D. Spin observable analysis

The parity-nonconserving nature of the weak decay of the Λ hyperons enables a determination of the Λ polarization by measuring the angular distribution of the decay protons. This normalized distribution may be written

$$I(\hat{p}_p) = \frac{1}{4\pi}(1 + \alpha \mathbf{P}_\Lambda \cdot \hat{p}_p),$$

where α is the $\Lambda \to p\pi^-$ weak decay asymmetry parameter having the measured value 0.642 ± 0.013 [40]. The vector polarization of the Λ is denoted by $\mathbf{P}_\Lambda$ and $\hat{p}_p$ represents the

direction vector of the decay proton in the Λ rest frame. In the $\bar{p}p \to \bar{\Sigma}^0\Lambda$ + c.c. reactions, the polarization transfer from the Σ to the daughter Λ in the electromagnetic decay of the Σ may be calculated and a similar form for the proton angular distribution results [41]:

$$I(\hat{p}_p) = \frac{1}{4\pi}\left(1 - \frac{1}{3}\alpha \mathbf{P}_\Sigma \cdot \hat{p}_p\right).$$

In this expression α is again the decay parameter of the Λ from the Σ-decay, $\mathbf{P}_\Sigma$ is the vector polarization of the Σ, and $\hat{p}_p$ is the direction vector of the decay proton in the Λ rest frame. The angular distribution of both decay protons in a $\bar{p}p \to \Lambda\bar{\Lambda}$ event may be written [41]:

$$I_{\Lambda\bar{\Lambda}}(\hat{p}_{\bar{p}}, \hat{p}_p) = \frac{1}{16\pi^2}\Big[1 + \bar{\alpha}\bar{\mathbf{P}}_{\bar{\Lambda}} \cdot \hat{p}_{\bar{p}} + \alpha \mathbf{P}_\Lambda \cdot \hat{p}_p + \bar{\alpha}\alpha \sum_{i,j} C_{ij}\, p_{\bar{p},i}\, p_{p,j}\Big],$$

where $\mathbf{P}_{\bar{\Lambda}}$, $\mathbf{P}_\Lambda$, and C_{ij} are, respectively, the $\bar{\Lambda}$, Λ vector polarizations, and the spin correlation coefficients. The $p_{\bar{p},i}$ and $p_{p,j}$ are the individual components of the $\bar{p}$ and p direction vectors as measured in the Λ and $\bar{\Lambda}$ rest frames. Similar expressions may be written for the $\bar{p}p \to \bar{\Sigma}^0\Lambda$ + c.c. reactions by correctly accounting for the Σ^0 and $\bar{\Sigma}^0$ decays.

From the angular distribution, the expectation values of the quantity $p_{p,j}$ are written

$$\langle p_{p,i} \rangle = \int\int p_{p,i} I_{\Lambda\bar{\Lambda}}(\hat{p}_{\bar{p}}, \hat{p}_p)\, d\Omega_{\bar{p}}\, d\Omega_p .$$

This integral is calculated yielding,

$$\langle p_{p,i} \rangle = \frac{1}{3}\alpha P_{\Lambda,i} .$$

Using this expression and the experimentally measured expectation value,

$$\langle p_{p,i} \rangle_{\text{expt}} = \frac{1}{N}\sum_{j=1}^{N} p_{p,i,j} ,$$

where N is the number of events in the experimental sample, yields the expression for the experimental estimate of the Λ polarization:

$$P_{\Lambda,i} = \frac{3}{\alpha N}\sum_{j=1}^{N} p_{p,i,j} .$$

Similar expressions result for the $\bar{\Lambda}$ polarization and the spin correlation coefficients.

However, when applied to experiment, the angular distributions are modified by the finite detector acceptance so that additional acceptance functions appear in these expressions. Fortunately, the physically interesting component of the hyperon polarization, P_y, the component perpendicular to the scattering plane,[1] is still easily extracted due to the symmetry of the detector acceptance for positive and negative values in the $\hat{y}$ direction. In this analysis, two coordinate systems are used. One is fixed in the hyperon rest frame and the other is in the antihyperon rest frame. The z axes are along the direction of motion of the respective hyperons in the c.m. and the y axes are normal to the production plane along a vector given by $\hat{p}_{\bar{p}} \times \hat{p}_{\bar{Y}}$. The x axes are then fixed by the requirement that the systems are right handed and orthogonal. The hyperon and antihyperon polarizations are measured in these systems. For the C_{ij}, i (j) labels the antihyperon (hyperon) component.

To extract the spin observables from the data, a ''method of moments'' was used, modified to incorporate the detector acceptance. With the consideration of finite detector acceptance, the angular distribution of the decay protons (written above) is multiplied by a detector acceptance function that depends on the directions of the outgoing decay protons ($p_{\bar{p},i}$ and $p_{p,j}$). Then, when the expectation value integrals are calculated and set equal to the experimental estimates, a system of coupled equations results with the spin observables and detector acceptances as the unknowns.

The physical constraints imposed by parity conservation on a subset of the spin observables were then used to eliminate some of the unknowns in the problem. The constraints are $P_{x,\bar{Y}} = P_{z,\bar{Y}} = P_{x,Y} = P_{z,Y} = 0$ and $C_{xy} = C_{yx} = C_{yz} = C_{zy} = 0$ [41]. With these additional constraints, the number of variables in the problem was reduced and the unknown acceptance functions could be extracted along with the remaining physically interesting spin observables, $P_{y,\bar{Y}}$, $P_{y,Y}$, C_{xz}, C_{zx}, C_{xx}, C_{yy}, and C_{zz}. Note that this spin-observable analysis is simulation independent; the effects of the finite detector acceptance are *measured* and *removed* from the physical distributions. For more details on this method see Ref. [36].

IV. RESULTS AND DISCUSSION

A. The $\bar{p}p \to \bar{\Lambda}\Lambda$ channel

At 1.726 and 1.771 GeV/c incident antiproton momentum, the excess kinetic energies available to the final-state hyperons in the reaction $\bar{p}p \to \Lambda\bar{\Lambda}$ are 103 and 119 MeV when averaged over the four target cells. The total cross sections at these two excess energies are measured to be $74.4 \pm 0.8 \pm 2.4$ and $79.9 \pm 0.9 \pm 2.6$ μb. The first error listed is statistical; each final data sample included approximately 10 000 events. The second is systematic and includes contributions from the average of the angular-dependent acceptance correction (2.3%), the uncertainty in the double-charged branching ratio (1.6%) and on the knowledge of the absolute luminosity (2.0%). The last of these includes uncertainties in the target cell corrections and in the carbon-event subtractions as well as in the overall beam flux. The systematic errors are combined in quadrature; the overall systematic error of 3.4% is the largest uncertainty in the total cross sections.

[1] For unpolarized beam and target the x and z components, which lie in the scattering plane, are required by parity conservation to be zero.

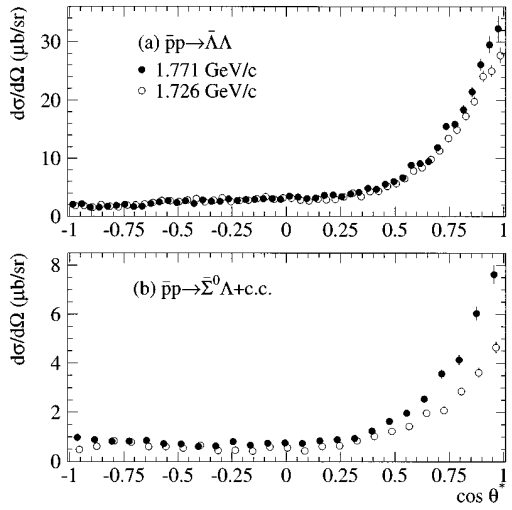

FIG. 6. Differential cross section results for the (a) $\overline{p}p \to \overline{\Lambda}\Lambda$ and (b) $\overline{p}p \to \overline{\Sigma}^0\Lambda$ + c.c. reactions at 1.726 and 1.771 GeV/c with horizontally offset points to avoid overlap. The angular-dependent systematic error (not included in indicated errors) is 2.3% for $\overline{p}p \to \overline{\Lambda}\Lambda$ and 3.6% for $\overline{p}p \to \overline{\Sigma}^0\Lambda$ + c.c. with strong bin to bin correlations. The systematic error on the scale is 2.6% for both plots.

The differential cross sections are shown in Fig. 6(a) as a function of $\cos\theta^*$, where θ^* is the c.m. angle of the outgoing $\overline{\Lambda}$. The data points are listed in Table I. The distributions are nearly identical at the two energies, apart from the increased slope for the higher-energy data at the very forward angles. This feature follows a consistent trend in the hyperon-antihyperon data that as the excess energy rises, the steepness of the forward slope increases. Evidently, larger numbers of partial waves begin to contribute as the energy increases from threshold. Under these circumstances, a theoretical analysis employing few partial waves is meaningful only in the low-energy regime.

One of the intriguing features of the $\overline{\Lambda}\Lambda$ data is the nonzero polarization of the outgoing hyperons which is observed at all energies with a consistently evolving shape versus energy. The data reported here are shown in Fig. 7(a) and represent two intermediate energies compared to our previously published work. The general trend in the differential polarization distributions includes a small positive polarization at forward angles, followed by a larger negative polarization at backward angles. For a given bin in $\cos\theta^*$ the polarization for the Λ and $\overline{\Lambda}$ should be identical (and are in our measurements); as such the averaged value is shown in the figure. At

TABLE I. Differential cross section values in 50 $\cos\theta^*$ bins for the $\overline{p}p \to \overline{\Lambda}\Lambda$ reaction at antiproton momenta of 1.726±0.001 and 1.771±0.001 GeV/c. Systematic and statistical errors are included.

		$\frac{d\sigma}{d\Omega}\left(\frac{\mu b}{sr}\right)$				$\frac{d\sigma}{d\Omega}\left(\frac{\mu b}{sr}\right)$	
Bin	$\cos\theta^*$	1.726 GeV/c	1.771 GeV/c	Bin	$\cos\theta^*$	1.726 GeV/c	1.771 GeV/c
1	-0.98	1.81±0.26	2.05±0.30	26	0.02	3.14±0.27	3.49±0.27
2	-0.94	1.89±0.23	2.16±0.27	27	0.06	2.81±0.26	3.31±0.26
3	-0.90	1.57±0.20	1.57±0.20	28	0.10	2.69±0.25	3.07±0.25
4	-0.86	2.02±0.22	1.56±0.19	29	0.14	2.99±0.26	3.21±0.26
5	-0.82	1.70±0.21	1.72±0.18	30	0.18	2.90±0.27	3.64±0.28
6	-0.78	1.60±0.20	1.88±0.21	31	0.22	2.95±0.27	3.71±0.28
7	-0.74	1.94±0.21	2.06±0.21	32	0.26	3.41±0.29	3.41±0.27
8	-0.70	1.99±0.22	1.67±0.19	33	0.30	4.04±0.31	3.89±0.29
9	-0.66	2.12±0.23	1.74±0.19	34	0.34	3.44±0.29	4.12±0.30
10	-0.62	2.35±0.24	2.24±0.22	35	0.38	4.30±0.33	4.84±0.34
11	-0.58	2.74±0.27	2.47±0.24	36	0.42	4.34±0.33	4.71±0.33
12	-0.54	2.69±0.25	2.72±0.24	37	0.46	5.19±0.37	5.59±0.36
13	-0.50	2.55±0.25	2.39±0.23	38	0.50	5.64±0.39	6.04±0.38
14	-0.46	2.81±0.27	2.70±0.24	39	0.54	6.55±0.42	6.66±0.41
15	-0.42	3.06±0.28	2.23±0.22	40	0.58	7.83±0.46	8.84±0.48
16	-0.38	2.45±0.24	2.85±0.25	41	0.62	8.41±0.48	9.12±0.48
17	-0.34	2.79±0.27	2.55±0.23	42	0.66	9.81±0.53	9.48±0.51
18	-0.30	3.19±0.28	2.57±0.23	43	0.70	11.34±0.58	11.92±0.58
19	-0.26	2.52±0.25	2.99±0.26	44	0.74	13.46±0.64	15.51±0.68
20	-0.22	2.74±0.26	2.72±0.23	45	0.78	14.93±0.70	15.90±0.71
21	-0.18	2.76±0.26	2.90±0.24	46	0.82	17.26±0.75	18.39±0.78
22	-0.14	3.01±0.28	2.95±0.24	47	0.86	19.80±0.83	21.45±0.89
23	-0.10	3.38±0.29	3.05±0.25	48	0.90	24.12±0.97	26.10±1.06
24	-0.06	2.95±0.26	3.05±0.26	49	0.94	24.99±1.06	29.52±1.39
25	-0.02	3.17±0.27	2.93±0.24	50	0.98	27.69±1.38	32.24±2.16

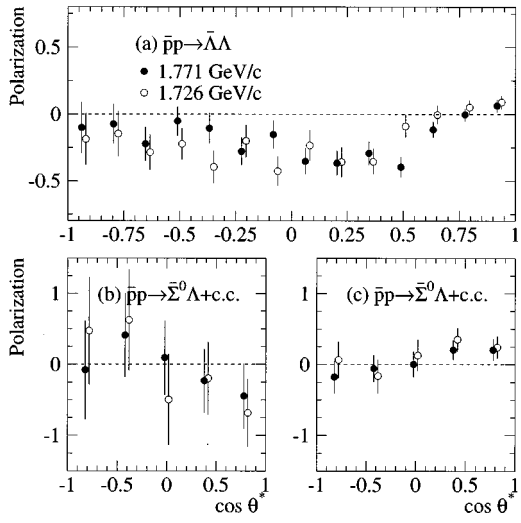

FIG. 7. Polarization of (a) the Λ and $\overline{\Lambda}$ for the $\overline{p}p\to\overline{\Lambda}\Lambda$ reaction, (b) the Σ^0 and $\overline{\Sigma}^0$, and (c) the Λ and Λ in the $\overline{p}p\to\overline{\Sigma}^0\Lambda+\text{c.c.}$ reactions at 1.726 and 1.771 GeV/c. The points have been offset horizontally to avoid overlap. Systematic errors are included.

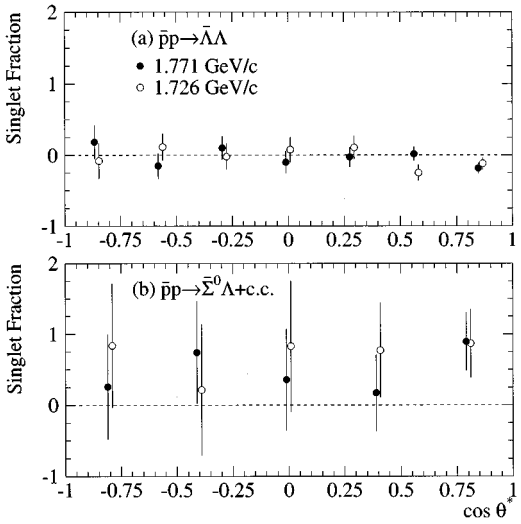

FIG. 8. Singlet fraction results for the (a) $\overline{p}p\to\overline{\Lambda}\Lambda$ and (b) $\overline{p}p\to\overline{\Sigma}^0\Lambda+\text{c.c.}$ reactions at 1.726 and 1.771 GeV/c. The points have been offset horizontally to avoid overlap. Systematic errors are included.

considerably higher excess energy (199 MeV) [5] a second node appears and the polarization at the very backward angles remains consistent with zero. The data reported here do not show the onset of these features.

Four of the spin correlation coefficients in the C_{ij} matrix are unique ($C_{xx}, C_{yy}, C_{zz}, C_{xz}$), not being constrained to zero nor representing reflections of one another. Values along the diagonal of the matrix, subdivided in the seven $\cos\theta^*$ bins, are combined to form a singlet fraction distribution following the prescription

$$S=\frac{1}{4}(1+C_{xx}-C_{yy}+C_{zz}).$$

Plots of S versus $\cos\theta^*$ are shown in Fig. 8(a). The errors in the plots have been propagated from the combinations of the contributing C_{ij} components. The angle-averaged singlet fractions are -0.08 ± 0.05 and -0.07 ± 0.05 for the 1.726 and 1.771 GeV/c data. This is entirely consistent with pure triplet production. Data entries for the polarization, spin correlation coefficients, and the singlet fraction are given in Table II.

B. The $\overline{p}p\to\overline{\Lambda}\Sigma^0+\text{c.c.}$ channel

The total cross sections for the $\overline{p}p\to\overline{\Sigma}^0\Lambda$ and $\overline{p}p\to\overline{\Lambda}\Sigma^0$ reactions must be equivalent according to charge conjugation invariance. At 1.726 GeV/c the measured cross sections are $6.99\pm0.19\pm0.31$ and $7.61\pm0.19\pm0.33$ μb for the $\overline{\Sigma}^0\Lambda$ and $\overline{\Lambda}\Sigma^0$ final states, respectively. At 1.771 GeV/c the results are $10.85\pm0.27\pm0.48$ and $10.37\pm0.24\pm0.46$ μb. The first errors given are statistical and are indicative of the event sample sizes; approximately 1500 events were extracted for each channel and at each energy. The second errors reflect systematic considerations. The slightly increased fractional systematic error here (4.4%) compared to the $\overline{\Lambda}\Lambda$ channel is entirely accounted for by additional uncertainty in the average angular acceptance function. The individual total cross sections are consistent, channel to channel, within the combined errors. We arrive at the final results for the combined $\overline{p}p\to\overline{\Sigma}^0\Lambda+\text{c.c.}$ channel:

$$\sigma(\overline{p}p\to\overline{\Lambda}\Sigma^0+\text{c.c.})=14.60\pm0.27\pm0.64\ \ \mu\text{b}$$

at 1.726 GeV/c, and

$$\sigma(\overline{p}p\to\overline{\Lambda}\Sigma^0+\text{c.c.})=21.22\pm0.36\pm0.93\ \ \mu\text{b}$$

at 1.771 GeV/c.

The cross-section ratio, R, between the $\overline{p}p\to\overline{\Sigma}^0\Lambda+\text{c.c.}$ and $\overline{p}p\to\overline{\Lambda}\Lambda$ reactions is of interest, particularly when made at the same excess energy because phase space differences are reduced and the comparison of FSI effects may be more appropriate. The ratio is defined as

$$R=\frac{\sigma(\Sigma^0\Lambda)}{\sigma(\overline{\Lambda}\Lambda)}=\frac{\sigma(\overline{\Sigma}^0\Lambda+\text{c.c.})/2}{\sigma(\overline{\Lambda}\Lambda}.$$

The results at $\epsilon=26$ and 40 MeV together with the previous measurement at $\epsilon=15$ MeV [35] have all been obtained at momenta which correspond to an excess energy matching that of a published $\overline{p}p\to\overline{\Lambda}\Lambda$ measurement. The cross-section ratios are summarized in Table III. The average value for R of 0.27 is consistent at all energies and is indicating that the respective reaction total cross sections ''turn on'' in very nearly the same way.

A first-order estimate of R can be made by comparing the ΣpK and ΛpK coupling constants and assuming that the ratio of reaction rates depends solely on respective kaon exchange strengths. Here, we have to assume that FSI interactions are similar and that differences in vector or tensor kaon exchanges are small. As mentioned ealier, ''realistic'' ratios

TABLE II. Spin observables in seven $\cos\theta^*$ bins for the $\overline{p}p \to \overline{\Lambda}\Lambda$ reaction at an average antiproton momentum of 1.726 ± 0.001 and 1.771 ± 0.001 GeV/c. F_s is the singlet fraction. Statistical and systematic errors are included.

		P_Λ@		C_{xx}@	
Bin	$\cos\theta^*$	1.726 GeV/c	1.771 GeV/c	1.726 GeV/c	1.771 GeV/c
1	-0.8571	-0.16 ± 0.14	-0.08 ± 0.14	-0.25 ± 0.55	-0.04 ± 0.54
2	-0.5714	-0.25 ± 0.09	-0.12 ± 0.09	-0.43 ± 0.49	-0.76 ± 0.47
3	-0.2857	-0.31 ± 0.09	-0.20 ± 0.08	-0.68 ± 0.56	-0.44 ± 0.49
4	0.0000	-0.33 ± 0.08	-0.25 ± 0.07	-0.09 ± 0.57	-0.66 ± 0.50
5	0.2857	-0.36 ± 0.07	-0.33 ± 0.06	1.19 ± 0.50	0.55 ± 0.41
6	0.5714	-0.04 ± 0.05	-0.22 ± 0.05	-0.21 ± 0.29	0.56 ± 0.26
7	0.8571	0.07 ± 0.04	0.03 ± 0.03	-0.33 ± 0.18	-0.53 ± 0.16
		C_{yy}@		C_{zz}@	
Bin	$\cos\theta^*$	1.726 GeV/c	1.771 GeV/c	1.726 GeV/c	1.771 GeV/c
1	-0.8571	0.12 ± 0.49	0.10 ± 0.44	-0.95 ± 0.72	-0.13 ± 0.64
2	-0.5714	-0.07 ± 0.35	-0.02 ± 0.32	-0.18 ± 0.48	-0.87 ± 0.46
3	-0.2857	0.28 ± 0.31	-0.13 ± 0.29	-0.13 ± 0.36	-0.29 ± 0.34
4	0.0000	0.56 ± 0.29	0.49 ± 0.27	-0.04 ± 0.31	-0.26 ± 0.28
5	0.2857	0.71 ± 0.28	1.06 ± 0.24	-1.07 ± 0.33	-0.60 ± 0.29
6	0.5714	0.84 ± 0.20	0.63 ± 0.19	-0.95 ± 0.29	-0.86 ± 0.25
7	0.8571	0.53 ± 0.15	0.58 ± 0.14	-0.62 ± 0.25	-0.63 ± 0.22
		C_{xz}@		F_s@	
Bin	$\cos\theta^*$	1.726 GeV/c	1.771 GeV/c	1.726 GeV/c	1.771 GeV/c
1	-0.8571	0.13 ± 0.45	0.08 ± 0.42	-0.08 ± 0.26	0.18 ± 0.24
2	-0.5714	0.03 ± 0.34	0.30 ± 0.32	0.11 ± 0.19	-0.15 ± 0.18
3	-0.2857	0.05 ± 0.31	0.04 ± 0.29	-0.02 ± 0.18	0.10 ± 0.17
4	0.0000	0.60 ± 0.30	0.52 ± 0.27	0.08 ± 0.18	-0.10 ± 0.16
5	0.2857	0.56 ± 0.28	0.52 ± 0.25	0.10 ± 0.16	-0.03 ± 0.14
6	0.5714	-0.45 ± 0.20	-0.27 ± 0.18	-0.25 ± 0.11	0.02 ± 0.10
7	0.8571	-0.27 ± 0.15	-0.29 ± 0.14	-0.12 ± 0.09	-0.19 ± 0.08

of the coupling constants can be obtained using SU(3) and a value for α of 0.355. Using these assumptions,

$$R = \frac{f^2_{\Sigma NK}}{f^2_{\Lambda NK}} \approx 0.08$$

which greatly underestimates the cross-section ratio.

In the coupled-channels meson-exchange calculation of Haidenbauer *et al.* [20], which includes both K and K^* exchange, the ratios of cross sections are adequately reproduced. They obtained a value of $R \approx 0.26$ to be compared to our $\epsilon = 15$ MeV result [35] and further predicted a ratio of 0.23 for the new 25 MeV data given here. When the authors turned off ISI and FSI effects (Born approximation), they predicted the same ratio we have given above, namely $R \approx 0.08$. This study demonstrates the critical nature of the FSI effects, which do not apparently drop out in such complete models when one is considering ratios of cross sections from different reactions.

However, in an evaluation using a quark dynamical model, Kohno and Weise [15] find a contradictory result by assuming that the FSI effects should be similar and thus do drop out in the ratio. They obtain the estimate of $R \approx 0.25$ which is consistent with our measurements and also to the available data at the time, stemming from considerably higher-energy experiments ($p_{\rm lab} \approx 2.5$ GeV/c, $\epsilon \approx 300$ MeV) [42].

TABLE III. Ratios of the total cross sections at three common excess energies.

ϵ (MeV)	$\sigma(\Sigma^0\Lambda)/\sigma(\overline{\Lambda}\Lambda)$	Ref. ($\overline{\Lambda}\Lambda$)	Ref. ($\Sigma^0\Lambda$)
≈ 15	0.29 ± 0.02	[3]	[35]
≈ 25	0.29 ± 0.02	[3]	This work
≈ 40	0.24 ± 0.02	[4]	This work

The differential cross sections for the combined events, $\overline{p}p \to \Lambda\overline{\Sigma}^0$+c.c., are shown in Fig. 6(b). The data, given also in Table IV, are binned in 25 equal spacings of $\cos\theta^*$ where θ^* is the c.m. scattering angle of the antihyperon. A characteristic of each distribution is the steep forward peaking which is found also in the $\overline{p}p \to \overline{\Lambda}\Lambda$ reaction. An interesting comparison of the $\overline{p}p \to \Lambda\overline{\Sigma}^0$+c.c. and $\overline{p}p \to \overline{\Lambda}\Lambda$ differential cross section shapes is made by examination of the distributions plotted versus t', the reduced four-momentum transfer. The quantity t' is defined as

TABLE IV. Differential cross section values in 25 $\cos\theta^*$ bins for the $\overline{p}p \to \overline{\Sigma}^0\Lambda + \text{c.c.}$ reaction at an average antiproton momenta of 1.726 ± 0.001 and 1.771 ± 0.001 GeV/c. Systematic and statistical errors are included.

		$\frac{d\sigma}{d\Omega}\left(\frac{\mu\text{b}}{\text{sr}}\right)$@	
Bin	$\cos\theta^*$	1.726 GeV/c	1.771 GeV/c
1	-0.96	0.48 ± 0.06	0.97 ± 0.10
2	-0.88	0.62 ± 0.08	0.89 ± 0.09
3	-0.80	0.83 ± 0.09	0.82 ± 0.09
4	-0.72	0.79 ± 0.09	0.82 ± 0.08
5	-0.64	0.60 ± 0.08	0.86 ± 0.08
6	-0.56	0.61 ± 0.08	0.73 ± 0.08
7	-0.48	0.54 ± 0.07	0.72 ± 0.08
8	-0.40	0.65 ± 0.08	0.62 ± 0.07
9	-0.32	0.45 ± 0.06	0.63 ± 0.07
10	-0.24	0.47 ± 0.07	0.81 ± 0.08
11	-0.16	0.43 ± 0.06	0.67 ± 0.07
12	-0.08	0.59 ± 0.07	0.75 ± 0.08
13	0.00	0.56 ± 0.07	0.76 ± 0.08
14	0.08	0.44 ± 0.06	0.74 ± 0.08
15	0.16	0.61 ± 0.07	0.85 ± 0.08
16	0.24	0.65 ± 0.08	0.90 ± 0.09
17	0.32	0.84 ± 0.09	0.94 ± 0.09
18	0.40	1.02 ± 0.10	1.24 ± 0.10
19	0.48	1.23 ± 0.11	1.63 ± 0.12
20	0.56	1.44 ± 0.12	1.97 ± 0.14
21	0.64	1.98 ± 0.14	2.55 ± 0.16
22	0.72	2.07 ± 0.14	3.57 ± 0.20
23	0.80	2.85 ± 0.17	4.14 ± 0.22
24	0.88	3.62 ± 0.20	6.03 ± 0.29
25	0.96	4.65 ± 0.24	7.62 ± 0.39

$$t' \equiv t - t_{\min} = 2pq(\cos\theta^* - 1),$$

where t is the four-momentum transfer (squared) and p and q are the incoming and outgoing c.m. momenta, respectively. In Fig. 9 the $\overline{p}p \to \Lambda\Lambda$ and $\overline{p}p \to \Lambda\overline{\Sigma}^0 + \text{c.c.}$ distributions are compared on the same plots at three comparable excess energies. A fit of the forward region using the exponential form $e^{-b|t'|}$ is superimposed and describes the data well. The functional form arises in the context of a simple black disk model; the slope b is related to the radius of the disk, r, by $b = r^2/4$. The slope for the $\overline{p}p \to \Lambda\overline{\Sigma}^0 + \text{c.c.}$ channel is consistently steeper (at the same excess energies) than that of the $\overline{p}p \to \Lambda\Lambda$ reaction, yielding values of 11–14 GeV^{-2} (1.3–1.5 fm) compared to 8–10 GeV^{-2} (1.1–1.2 fm) for the $\Lambda\Lambda$ channel [43].

The polarization of the outgoing Λ or Σ hyperon has been determined as a function of the respective hyperon c.m. scattering angle. These plots are shown in Figs. 7(b) and 7(c). The shape of the Λ polarization is similar to that observed in the reaction $\overline{p}p \to \Lambda\Lambda$; it features a positive polarization at forward angles, a crossing of zero, and a slight negative polarization in the backward direction. The Σ polarization is much harder to determine because of the larger errors that result due to the factor of $-\frac{1}{3}$ that arises due to the Σ^0 decay. Nevertheless, one can see a consistent trend in the data for both energies which features a behavior which is nearly opposite in sign to the Λ polarization.

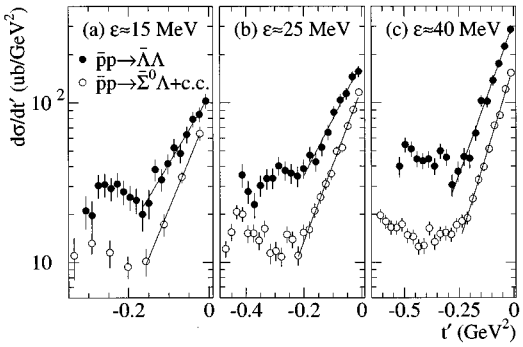

FIG. 9. Differential cross section comparison of $\overline{p}p \to \overline{\Lambda}\Lambda$ and $\overline{p}p \to \overline{\Sigma}^0\Lambda + \text{c.c.}$ at three common excess energies. The data are plotted vs t', the reduced four-momentum transfer squared. The solid lines are the result of fits to an exponential form in the forward regions. Data in (a) have been reported in [3,35]. The $\overline{\Lambda}\Lambda$ data in (b) are from [3] and in (c) are from [4].

While the polarization information can be extracted from the study of either of the hyperons separately, the spin correlation coefficients are determined from the combined decay information. Due to the increased uncertainty on the $\overline{\Sigma}^0$ side, the errors are significanly larger than for the $\overline{\Lambda}\Lambda$ channel. However, the C_{ij} information for the five nonzero distributions ($C_{xx}, C_{yy}, C_{zz}, C_{xz}$, and C_{zx}) is consistent at both energies and leads to a meaningful extraction of the singlet fraction. Here, C_{xz} can be different from C_{zx}, unlike the $\overline{\Lambda}\Lambda$ case. The singlet fraction is computed from the diagonal elements and results in the distributions shown in Fig. 8(b). The singlet fractions differ from zero which is indicative of combined singlet and triplet production at each of the energies. The angle-averaged value for S is 0.76 ± 0.31 at 1.726 GeV/c and 0.56 ± 0.26 at 1.771 GeV/c. The polarization, spin correlation coefficient, and singlet fraction data are given in Table V.

These nontriplet results are consistent with the quark model prediction of $S = \frac{3}{7}$ that results from a vector [26] or scalar [31] $\overline{ss}$ quark pair production mechanism. Haidenbauer *et al.* have calculated [20] a singlet fraction value of 0.2 at 1.695 GeV/c ($\epsilon = 15$ MeV). The evolution of S with increasing energy is not discussed by the authors, but is a relatively static property in the $\overline{\Lambda}\Lambda$ case until about $\epsilon = 200$ MeV where the first deviations from pure triplet production are observed [5].

V. CONCLUSIONS

The goal of the PS185 collaboration is to establish the definitive $\overline{p}p \to \overline{Y}Y$ data set in the low-energy regime. From theoretical analysis of the data, one hopes to gain insight into the behavior of hadron interactions at intermediate energies. This is in an energy regime where perturbative QCD is inappropriate and both quark-gluon and meson degrees of freedom are believed to be important.

The measurements reported here extend the data on the

TABLE V. Spin observables in five $\cos\theta^*$ bins for the $\overline{p}p \to \overline{\Sigma}^0\Lambda$ + c.c. reaction at an average antiproton momentum of 1.726 ± 0.001 GeV/c and 1.771 ± 0.001 GeV/c. F_s is the singlet fraction. Statistical and systematic errors are included.

		P_{Σ^0} @		P_Λ @	
Bin	$\cos\theta^*$	1.726 GeV/c	1.771 GeV/ c	1.726 GeV/c	1.771 GeV/c
1	-0.80	0.47 ± 0.75	-0.08 ± 0.69	0.07 ± 0.25	-0.18 ± 0.23
2	-0.40	0.62 ± 0.70	0.41 ± 0.60	-0.16 ± 0.24	-0.06 ± 0.19
3	0.00	-0.50 ± 0.65	0.09 ± 0.53	0.13 ± 0.22	0.00 ± 0.18
4	0.40	-0.20 ± 0.51	-0.23 ± 0.45	0.35 ± 0.17	0.20 ± 0.14
5	0.80	-0.66 ± 0.46	-0.45 ± 0.45	0.25 ± 0.15	0.20 ± 0.15
		C_{xx} @		C_{yy} @	
Bin	$\cos\theta^*$	1.726 GeV/c	1.771 GeV/ c	1.726 GeV/c	1.771 GeV/c
1	-0.80	2.08 ± 1.99	-0.57 ± 1.70	0.20 ± 1.70	0.46 ± 1.49
2	-0.40	-0.57 ± 2.70	0.14 ± 2.02	-1.52 ± 1.66-	-0.72 ± 1.38
3	0.00	3.41 ± 2.84	1.58 ± 2.17	0.11 ± 1.58	0.43 ± 1.27
4	0.40	0.06 ± 1.90	0.45 ± 1.51	-0.79 ± 1.20	1.64 ± 1.05
5	0.80	1.14 ± 1.00	0.39 ± 0.94	0.80 ± 1.02	-0.95 ± 0.85
		C_{zz} @		C_{xz} @	
Bin	$\cos\theta^*$	1.726 GeV/c	1.771 GeV/ c	1.726 GeV/c	1.771 GeV/c
1	-0.80	0.41 ± 2.31	1.05 ± 1.93	0.50 ± 2.01	-0.15 ± 1.75
2	-0.40	-1.07 ± 1.88	1.11 ± 1.55	0.97 ± 2.04	-1.32 ± 1.70
3	0.00	-0.97 ± 1.76	-0.72 ± 1.39	0.76 ± 2.20	0.66 ± 1.69
4	0.40	1.24 ± 1.45	0.87 ± 1.15	1.11 ± 1.63	-0.08 ± 1.25
5	0.80	0.89 ± 0.42	1.24 ± 1.08	-0.66 ± 0.46	1.14 ± 1.00
		C_{zx} @		F_s @	
Bin	$\cos\theta^*$	1.726 GeV/c	1.771 GeV/ c	1.726 GeV/c	1.771 GeV/c
1	-0.80	-0.28 ± 2.07	-0.27 ± 1.84	0.82 ± 0.87	0.26 ± 0.74
2	-0.40	1.86 ± 2.38	-0.52 ± 1.72	0.22 ± 0.92	0.74 ± 0.72
3	0.00	1.37 ± 2.27	2.09 ± 1.75	0.83 ± 0.92	0.36 ± 0.72
4	0.40	0.25 ± 1.76	0.98 ± 1.34	0.77 ± 0.67	0.17 ± 0.54
5	0.80	0.25 ± 0.15	0.80 ± 1.02	0.47 ± 0.15	0.89 ± 0.42

well-measured $\overline{p}p \to \overline{\Lambda}\Lambda$ channel and greatly increase what has been known about the complementary $\overline{p}p \to \overline{\Lambda}\Sigma^0$ + c.c. reactions. In particular, the large number of $\overline{p}p \to \overline{\Lambda}\Sigma^0$ + c.c. events has enabled extraction of the outgoing Λ and Σ polarizations, the spin correlation coefficients and, from these, the first determination of the singlet fraction.

Comparison of the $\overline{p}p \to \overline{\Lambda}\Sigma^0$ + c.c. to the $\overline{p}p \to \overline{\Lambda}\Lambda$ channel at common excess energies has been presented and yields the following significant findings.

(1) The ratio of total cross sections, $R = \sigma(\Sigma^0\Lambda)/\sigma(\Lambda\Lambda) \approx 0.27$, appears to be independent of excess energy in the low energy regime studied here.

(2) The differential cross sections for the $\overline{p}p \to \Lambda\Sigma^0$ + c.c. reactions feature the onset of higher partial waves earlier in excess energy as compared to the $\overline{p}p \to \Lambda\Lambda$ reaction.

(3) The Λ polarization structure is similar to that found in the $\overline{p}p \to \Lambda\Lambda$ reaction; the Σ polarization, although more poorly determined, indicates a behavior opposite in sign to the Λ.

(4) The angle- and energy-averaged singlet fraction for $\overline{p}p \to \Lambda\Sigma^0$ + c.c. is $S = 0.64 \pm 0.20$ which indicates that it is highly probable that both singlet and triplet production mechanisms are involved; for the $\overline{p}p \to \Lambda\Lambda$ reaction, only triplet production is observed in this energy regime.

An important result stemming from earlier PS185 data on the $\overline{p}p \to \overline{\Lambda}\Lambda$ reaction was the determination of the coupling constant $f_{\Lambda NK}$ in the context of the Nijmegen partial wave analysis [6]. A strong motivation for increasing the number of data points in the complementary reaction $\overline{p}p \to \Lambda\Sigma^0$ + c.c. is to enable a comparable treatment in order to extract a value for $f_{\Sigma NK}$. Using our preliminary 1.726 GeV/c data, coupled with additional PS185 data, an update of the coupling constant extraction was reported by Timmermans [44]. The values $f^2_{\Lambda NK}/4\pi = 0.069(4)$ and $f^2_{\Sigma NK}/4\pi = 0.005(2)$ were obtained. With the inclusion of this more complete data set on $\overline{p}p \to \overline{\Lambda}\Sigma^0$ + c.c. we expect the precision on $f_{\Sigma NK}$ to improve such that a meaningful comparison of the coupling constants can be made, even to the level of possibly demonstrating SU(3) breaking [45].

ACKNOWLEDGMENTS

The members of the PS185 collaboration thank the LEAR accelerator team for the excellent preparation of the antiproton beam. Two of us (R.L.T. and D.W.H.) would like to thank R. Timmermans for numerous fruitful discussions during the course of this work. We also gratefully acknowledge financial and material support from the German Bundesministerium für Bildung und Forschung, the Swedish Natural Science Research Council, the United States Department of Energy under Contract No. DE-FG02-87ER40315, and the United States National Science Foundation under Contract No. NSF PHY-93-10871. This work was based in part on the dissertation of R. Tayloe, submitted to the University of Illinois in partial fulfillment of the requirements for the Ph.D. degree.

[1] P. D. Barnes *et al.*, Phys. Lett. B **229**, 432 (1989).
[2] P. D. Barnes *et al.*, Phys. Lett. B **331**, 203 (1994).
[3] P. D. Barnes *et al.*, Phys. Lett. B **189**, 249 (1987).
[4] P. D. Barnes *et al.*, Nucl. Phys. **A526**, 575 (1991).
[5] P. D. Barnes *et al.*, Phys. Rev. C **54**, 1877 (1996).
[6] R. Timmermans, T. Rijken, and J. de Swart, Phys. Lett. B **257**, 227 (1991).
[7] P.D. Barnes *et al.*, Phys. Lett. B **199**, 147 (1987).
[8] R. Timmermans, T. Rijken, and J. de Swart, Nucl. Phys. **A479**, 383c (1988); Phys. Rev. D **45**, 2288 (1992).
[9] A. Kudriyavtsev and V. Samoilov, Mod. Phys. Lett. A **4**, 721 (1989).
[10] F. Tabakin, R. A. Eisenstein, and Y. Lu, Phys. Rev. C **44**, 1749 (1991).
[11] A. Schneider-Neureither *et al.*, Z. Phys. A **344**, 317 (1993).
[12] F. Tabakin and R. A. Eisenstein, Phys. Rev. C **31**, 1857 (1985).
[13] A. Green and J. Niskanen, Prog. Part. Nucl. Phys. **18**, 93 (1987).
[14] M. Kohno and W. Weise, Phys. Lett. B **179**, 15 (1986); **206**, 584 (1988).
[15] M. Kohno and W. Weise, Nucl. Phys. **A479**, 433c (1988).
[16] W. Weise, Nuc. Phys. **A558**, 219c (1993).
[17] P. LaFrance and B. Loiseau, Nucl. Phys. **A528**, 557 (1991); P. LaFrance, B. Loiseau, and R. Vinh Mau, Phys. Lett. B **214**, 317 (1988).
[18] Y. Lu and M. Locher, Z. Phys. A **346**, 143 (1993).
[19] J. Haidenbauer *et al.*, Phys. Rev. C **45**, 931 (1992).
[20] J. Haidenbauer *et al.*, Phys. Rev. C **46**, 2516 (1992).
[21] J. Haidenbauer *et al.*, Phys. Lett. B **291**, 223 (1992); Phys. Rev. C **46**, 2158 (1992).
[22] M. Alberg, E. Henley, and L. Wilets, Z. Phys. A **331**, 207 (1988); Phys. Rev. C **38**, 1506 (1988).
[23] M. Alberg, E. Henley, and W. Weise, Phys. Lett. B **255**, 498 (1991).
[24] M. Alberg, E. M. Henley, L. Wilets, and P. D. Kunz, Nucl. Phys. **A560**, 365 (1993).
[25] M. Alberg, E. M. Henley, L. Wilets, and P. D. Kunz, Phys. Atom. Nucl. **57**, 1608 (1994).
[26] H. Genz and S. Tatur, Phys. Rev. D **30**, 63 (1984).
[27] G. Brix, H. Genz, and S. Tatur, Phys. Rev. D **39**, 2054 (1989).
[28] P. Kroll and W. Schweiger, Nucl. Phys. **A474**, 608 (1987).
[29] P. Kroll, B. Quadder, and W. Schweiger, Nucl. Phys. **B316**, 373 (1989).
[30] H. Genz, M. Nowakowski, and D. Woitschitzky, Phys. Lett. B **260**, 179 (1991).
[31] S. Furui and A. Faessler, Nucl. Phys. **A468**, 669 (1987).
[32] M. Burkhardt and M. Dillig, Phys. Rev. C **37**, 1362 (1988).
[33] W. Roberts, Z. Phys. C **49**, 633 (1991).
[34] H. Rubinstein and H. Snellman, Phys. Lett. B **165**, 187 (1985).
[35] P. D. Barnes *et al.*, Phys. Lett. B **246**, 273 (1990).
[36] R.L. Tayloe, Ph.D. thesis, University of Illinois, Urbana-Champaign, 1995.
[37] Application Software Group, Computing and Networks Division, GEANT Detector Description and Simulation Tool, CERN, Geneva, Switzerland, 1993.
[38] S. Ohlsson, Ph.D. thesis, Uppsala University, 1986.
[39] V. P. Zhigunov, Nucl. Instrum. Methods **216**, 183 (1983).
[40] Particle Data Group, Phys. Rev. D **50**, 1 (1994).
[41] L. Durand and J. Sandweiss, Phys. Rev. **135B**, 540 (1964).
[42] J. Badier, A. Bonnet, P. Briandet, and B. Sadoulet, Phys. Lett. **25B**, 152 (1967).
[43] The comparison of the forward slopes of two-body inelastic reactions using this simple fitting procedure is discussed in M. L. Perl, *High Energy Hadron Physics* (Wiley, New York, 1974) Secs. 7-4 and 7.5.
[44] R. Timmermans, T. Rijken, and J. de Swart, Nucl. Phys. **A585**, 143c (1995).
[45] R. Timmermans (private communication).